Nano Energy 50 (2018) 176–181

Contents lists available at ScienceDirect

Nano Energy

journal homepage: www.elsevier.com/locate/nanoen

Full paper

Colloidal synthesis of 1T' phase dominated WS_2 towards endurable electrocatalysis

Zhengqing Liu[a], Na Li[b], Cong Su[c], Hongyang Zhao[b], Lingling Xu[b], Zongyou Yin[d,*], Ju Li[c,*], Yaping Du[a,b,*]

[a] School of Materials Science and Engineering & National Institute for Advanced Materials, Nankai University, Tianjin 300350, China
[b] Frontier Institute of Science and Technology, Xi'an Jiaotong University, Xi'an 710049, China
[c] Department of Nuclear Science and Engineering and Department of Materials Science and Engineering, Massachusetts Institute of Technology, Cambridge, MA 02139, USA
[d] Research School of Chemistry, The Australian National University, Canberra, Australian Capital Territory 2601, Australia

ARTICLE INFO

Keywords:
Colloidal synthesis
Hydrogen evolution
1T′ phase WS_2
Endurance half-life
Erosion

ABSTRACT

Transition metal dichalcogenide (TMD) nanomaterials have attracted tremendous attention due to their great potential for hydrogen evolution reaction (HER), especially with their metallic 1T/1T′ phase, which possesses much higher HER activity than the 2H phase. But the metallic phase can transform to 2H phase accompanied by an undesirable degradation in HER activity. Currently, how to prepare the stable metallic phase TMD nanomaterials enabling an endurable HER is one of the main challenges for practical application. Herein, we establish an effective colloidal chemistry strategy for the controllable synthesis of metallic 1T′ phase dominated WS_2 (1T′-D WS_2) nanostructures. Such 1T′-D WS_2 exhibits higher performance and more stable HER activity than 2H phase WS_2 in the H_2SO_4 electrolyte. The endurance half-life of 1T′-D WS_2 from stability testing under constant overpotential of 0.3 V vs. RHE and an initial current density of 41 mA/cm^2 is about 46 days, despite vigorous erosion due to continuous H_2 bubbling which exerts large capillary stresses on the atomic sheets. The facile preparation of highly stable 1T′-phase dominated TMD nanomaterials advances them as competitive sustainable HER electrocatalysts.

1. Introduction

Hydrogen evolution reaction (HER) through electrocatalysis is considered a key reaction for clean energy conversion [1]. Platinum (Pt) on carbon is the standard electrocatalyst, but earth's Pt resources might be insufficient if electrolyzer and fuel cell technologies are scaled up [2]. Huge efforts have been devoted to preparing non-Pt electrocatalysts with the enhanced HER performance. In recent years, among the non-Pt electrocatalysts, the layered transition metal dichalcogenide (TMD) nanomaterials, such as MoS_2 and WS_2, especially their metallic (1T/1T′) phase [3–5], are considered promising candidates for HER electrocatalyst [3–9]. For instance, experimental studies have shown that the 1 T phase MoS_2 and WS_2 fabricated from the lithium exfoliation method exhibited enhanced HER electrocatalytic performance compared to the corresponding 2H phase [3,4]. Chou et al. [10] confirmed that 1T′ MoS_2 was the relatively more active phase towards HER since its active sites are distributed on both the basal planes and the edges, rather than just the edges of the 2H phase MoS_2. On account of this, different fabrication methods have been investigated for preparation of the metallic phase TMD nanomaterials, including chemical exfoliation [3,4,11], solvothermal [12,13] and colloidal chemistry [14]. However, the aforementioned methods on the synthesis of the metallic phase TMD nanomaterials were restricted to incremental improvement on the cost and/or activity, but without addressing the stability issue. The nondurable performance is associated with the unstable features of metallic phase TMD nanomaterials, which easily transform to 2H phase, accompaning the undesirable degradation of catalytic activity [2,15]. We would therefore like to develop an effective strategy which not only can prepare high-ratio metallic phase of TMD nanomaterials but also can prevent the metallic phase transformation to 2H phase in water/air.

As an important member of layered TMD compounds, tungsten disulfide (WS_2) has wide applications in lubrication [16], field effect transistors [17], electrocatalysis [6] and photocatalysis [14,18]. However, the metallic phase WS_2 nanostructures, especially the 1T′ phase, is much less explored. Recently, colloidal chemical synthesis was demonstrated to work impressively in that it retained the stability of synthesized metallic phase MoS_2 over 3 months, much longer than 12 days of chemically exfoliated MoS_2, which can reverse-transform from

* Corresponding authors.
E-mail addresses: zongyou.yin@anu.edu.au (Z. Yin), liju@mit.edu (J. Li), ypdu@nankai.edu.cn (Y. Du).

https://doi.org/10.1016/j.nanoen.2018.05.019
Received 21 February 2018; Received in revised form 7 May 2018; Accepted 7 May 2018
Available online 09 May 2018

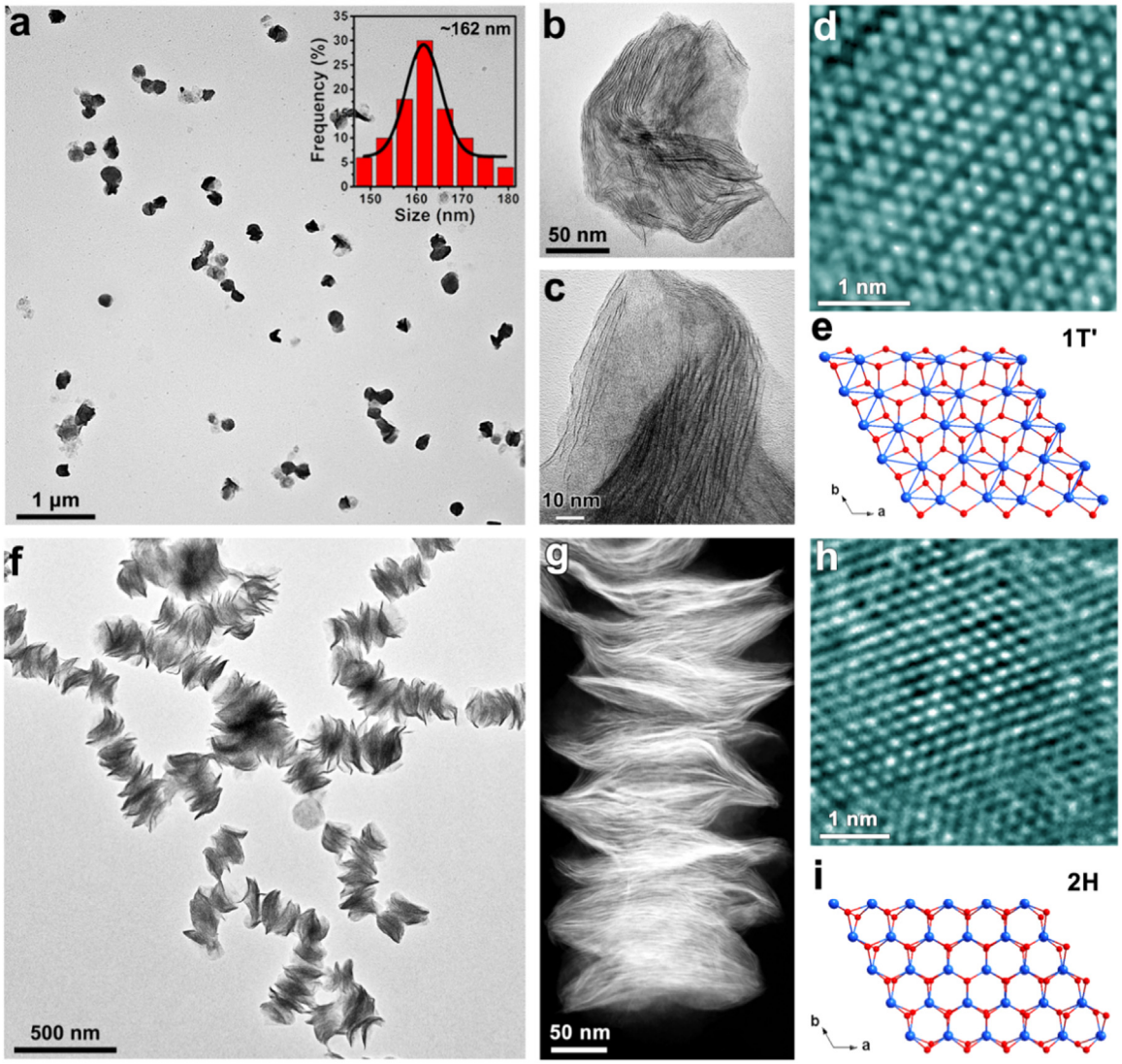

Fig. 1. (a) Typical low magnified TEM image of WS_2 NPs with a dominant size of ~ 162 nm (inset of a). (b) A single TEM image and (c) enlarged TEM image of the WS_2 nanoparticles (NP). HRTEM image of (d) WS_2 NPs, and (e) c-axis view of WS_2 NPs predicted based on structural optimization of the unit cell. Red and blue balls represent S and W atoms, respectively. (f) TEM and (g) HAADF-STEM images of WS_2 nanochains (NCs). HRTEM image of (h) WS_2 NCs and corresponding (I) c-axis view of atomic structure model.

1T to 2H [19–21]. Herein, we established a facile and effective one-pot colloidal chemical strategy to selectively synthesize stable 1T′ phase dominated (mixed with 2H phase) and pure 2H phase (as control) WS_2 nanostructures, respectively, abbreviated to 1T′-D WS_2 and 2H WS_2. Compared to 2H WS_2, 1T′-D WS_2 exhibited superior HER performance, such as low overpotential of 200 mV at the current density (J) of 10 mA/cm^2, small Tafel slope of 50.4 mV/dec and excellent stability. As a proof-of-concept demonstration, a HER endurance half-life of 46 days from of 1T′-D WS_2 was first extracted by performing ultralong HER operation at static overpotential.

2. Results and discussion

The 1T′-D WS_2 was prepared by our one-pot colloidal synthesis approach (see details in Supporting Information). Briefly, 0.2 mmol $(NH_4)_2WO_4$ and 0.6 mmol thiourea in 20 mmol oleylamine (OM) were used for reaction at 280 °C for 90 min. As shown in the scanning electron microscope (SEM) image of Fig. S1a, the WS_2 sample has nanoparticle-like (NP) structure. The typical low-magnification transmission electron microscopy (TEM) image (Fig. 1a) shows the as-prepared WS_2 nanoparticles (NPs) are relatively monodisperse with a dominant size of ~ 162 nm (inset histogram of Fig. 1a), suggesting the retention of capping ligands on the surface of nanostructures, as verified by Fourier transform infrared (FTIR) spectroscopy (Fig. S1b). The magnified morphology of an individual WS_2 NP (Fig. 1b and Fig. S1c–f) reveals that the entire WS_2 NP comprises of closely-stacked thin nanosheets, which is more discernible in the enlarged TEM image (Fig. 1c). The energy-dispersive X-ray spectroscopy (EDX) (Fig. S1g) confirms that stoichiometric WS_2 is formed with an atomic ratio of W/S ≈ 1/2, consistent with the inductive coupled plasma-optical emission spectroscopy (ICP-OES) data of 1/2.07. The detailed crystal structure of WS_2 NP was examined by high-resolution TEM (HRTEM, Fig. 1d), which was recorded from the planar orientation. It indicates that the crystal lattice of the synthesized WS_2 NP is dominated by the distorted 1T′ phase structure with a feature of a zigzag chain of W atoms [4,14], which is consistent with the *c*-axis view of its corresponding atomic structure model (Fig. 1e). The ratio of 1T′ phase vs 2H phase will be analyzed in the following section.

In addition, under the same conditions, except that 16 mmol OM and 4 mmol oleic acid (OA) were used as solvents for reaction at 280 °C for 60 min, our WS_2 features self-assembled chain-like nanostructures. The obvious ripples and corrugations shown in Fig. 1f,g and Fig. S2a

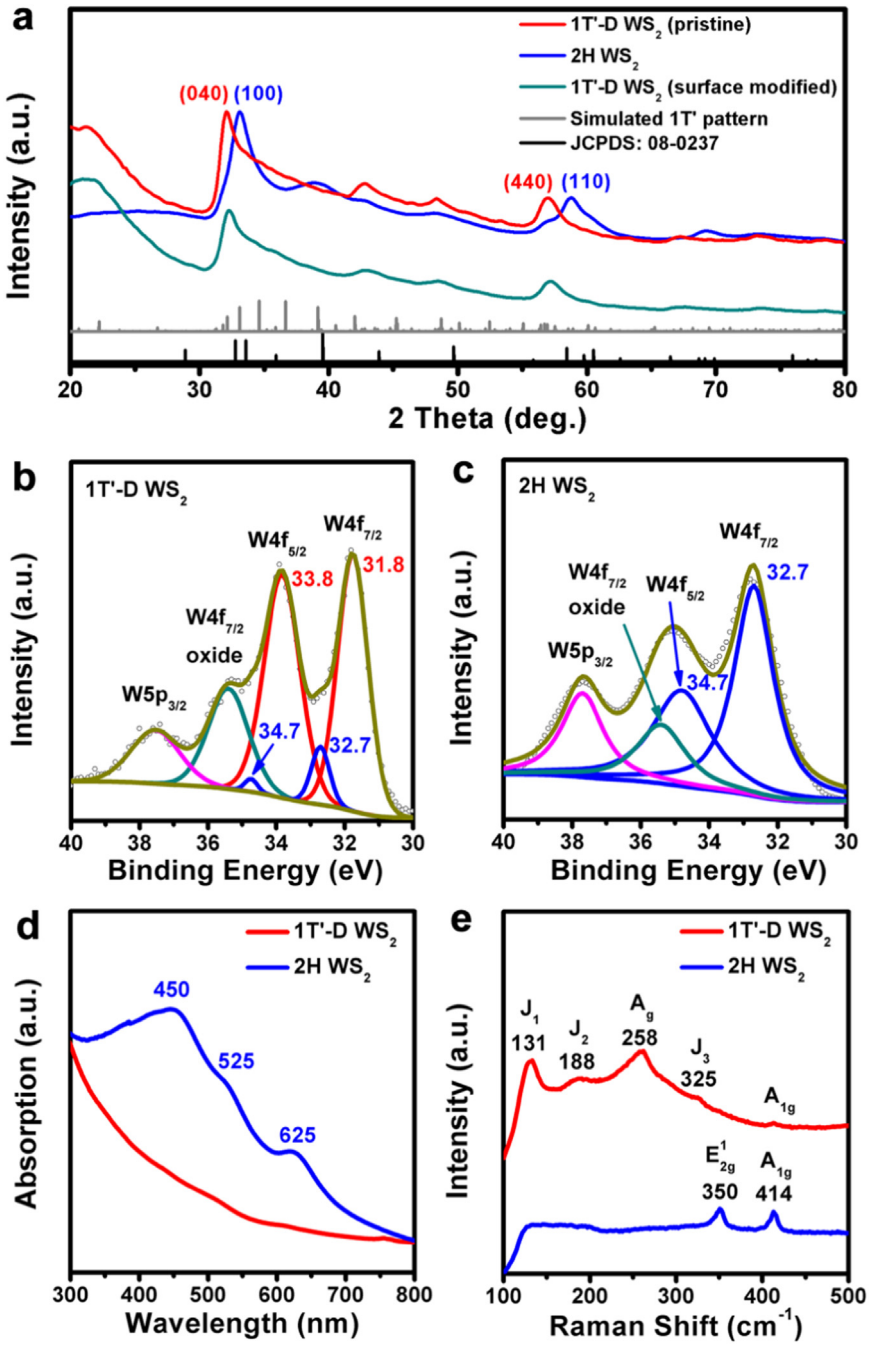

Fig. 2. (a) XRD patterns of pristine 1T′-D WS_2 nanoparticles (NPs), after surface modified 1T′-D WS_2 NPs and 2H WS_2 NCs. (b,c) XPS spectra of W signals recorded from 1T′-D WS_2 NPs and 2H WS_2 nanochains (NCs), respectively. (d) UV–vis spectra and (e) Raman spectroscopy of as-obtained 1T′-D WS_2 NPs and 2H WS_2 NCs samples.

suggest the WS_2 nanochains (NCs) were constructed from WS_2 nanosheets with a thickness of ~ 7.6 nm (about 11 WS_2 monolayers). The FTIR spectroscopy indicates the retention of OM and OA capping ligands on the WS_2 NCs surfaces (Fig. S2b). The HRTEM image (Fig. 1h) clearly shows the crystal structure of the WS_2 NCs is hexagonal, indexed to 2H phase WS_2 [3]. Viewed from the *c*-axis of atomic structure model (Fig. 1i), the 2H phase WS_2 hold the regular hexagonal structure feature, consistent with the HRTEM image.

X-ray diffraction (XRD) patterns, X-ray photoelectron spectroscopy (XPS), UV–vis and Raman scattering were used to further identify the 1T′ and 2H phase of WS_2 nanostructures. The XRD patterns of WS_2 NPs and WS_2 NCs samples are presented in Fig. 2a, and both exhibit well-resolved diffraction peaks. The XRD peaks in regions of 31–32° and 56–59° can be used to identify 1T′ phase or 2H phase WS_2. As shown in Fig. 2a, the XRD peaks of WS_2 NPs at 31.9° and 56.7° correspond to the (040) and (440) planes of the 1T′ phase, while the peaks of WS_2 NCs at 32.9° and 58.5° correspond to the (100) and (110) planes of the 2H phase. In order to further confirm our conclusion, we annealed the WS_2 NPs at 200 °C for 2 h under the protection of N_2. During the thermal treatment, it was found that the XRD peaks at 31.9° and 56.7° of WS_2 NPs gradually shifted to 32.9° and 58.5° of 2H phase, as shown in Fig. S3a,b.

The core level peaks of $W4f_{7/2}$ and $W4f_{5/2}$ in XPS spectra is an efficient way to distinguish the metallic and 2H phase. As shown in Fig. 2b, double peaks located at 31.8 eV and 33.8 eV are ascribed to the core levels of $W4f_{7/2}$ and $W4f_{5/2}$ of 1T′ phase WS_2, respectively

[4,12,14]. The ratio of 1T′ phase and 2H phase occupies 66.4% and 5.8% in WS_2 NPs sample, respectively, indicating the formation of 1T′-D WS_2 nanocrystals. Two strong peaks of WS_2 NCs at 32.7 eV ($W4f_{7/2}$) and 34.7 eV ($W4f_{5/2}$) (Fig. 2c) are the characteristics of W for 2H phase WS_2, and 2H phase occupies 62% in WS_2 NCs sample. Meanwhile, the peaks at 37.5 eV and 35.4 eV corresponding to $W5p_{3/2}$ and $W4f_{7/2}$ (Fig. 2b,c) for both WS_2 samples can also be observed, which may originate from amorphous WO_x-like clusters on the surface of as-prepared WS_2 nanostructures [14]. The ratio of WO_x was 27.8% and 38% in the synthesized 1T′-D and 2H WS_2 samples, respectively. The UV–vis absorption spectra (Fig. 2d) give similar results to previously reported TMD nanocrystals, revealing the 1T′ phase for WS_2 NPs and the 2H phase for WS_2 NCs (characteristic peaks at ~ 450 nm, 525 nm and 625 nm) [14]. The Raman shifting peaks of WS_2 NCs at 350 cm^{-1} and 414 cm^{-1} are observed (Fig. 2e), which are attributed to E^1_{2g} and A_{1g} of the characteristic 2H phase. The obviously different Raman shifting peaks of WS_2 NPs located at 131 cm^{-1}, 188 cm^{-1}, 258 cm^{-1} and 325 cm^{-1} in the lower frequency region correspond to J_1, J_2, A_g and J_3 peaks, respectively, unambiguously confirming the formation of 1T′ phase WS_2 NPs [4,12].

The optimal reaction parameters for colloidal synthesis of 1T′-D WS_2 and 2H WS_2 were screened, such as precursor concentration and the ratio of OM/OA surfactants, as detailed in the supporting information (Figs. S4 and S5). Normally, the phase of nanocrystals can be controlled by tuning the surfactants during the colloidal synthesis process [14,22]. In the present work, the combination of different surfactants was found to play a key role in obtaining 1T′-D WS_2 and 2H WS_2. Sole use of OM as surfactant produced 1T′-D WS_2. Notably, when adding a little amount of OA, the 1T′-D WS_2 would change to 2H phase. The reason for forming different phases of WS_2, changing from 1T′ phase to 2H phase, can be explained by electrostatic interactions between the surface charge of $[WS_2]^-$ species and the surfactants used [14,23]. For 1T′-D WS_2, the negatively charged $[WS_2]^-$ species can be stabilized by the positively charged OM surfactant because of their strong interactions. For 2H WS_2, the added OA surfactant weakens the electrostatic interactions, which cannot prevent its transformation to the thermodynamically stable 2H phase. This can be further confirmed by the thermal treatment results (Fig. S3), the OM surfactant interaction with the 1T′-D WS_2 becomes less important with increasing temperature and leads to the transformation from 1T′ phase to 2H phase.

There are three key known factors for achieving excellent HER electrocatalytic activity: active sites, intrinsic conductivity and clean surface. In order to generate a hydrophilic surface for electrocatalysis, we employed acid treatment to remove/modify the surfactant molecules at synthesized WS_2 nanostructures (see details in the experimental section of supporting information) [23,24]. Our experimental results showed that the 1T′-D WS_2 still remained in 1T′ phase after acid treatment, which was confirmed by XRD pattern (Fig. 2a) and XPS spectra of W4f (Fig. S6a). This is ascribed to large adsorption energy of thioglycollic acid on 1T′-D WS_2 [23]. Note here, however, the 2H WS_2 changed to oxide (Fig. S6b) under the same condition probably due to the weak interaction between 2H WS_2 and thioglycollic acid, which does not give protection [23]. From above analysis, we can find that our synthesized 1T′-D WS_2 was more stable than 2H WS_2 during the surface modification process, which paved the way for the electrocatalysis applications.

The as-prepared 1T′-D WS_2 and 2H WS_2 were used to investigate the HER electrocatalytic performances. As shown in Fig. 3a, the polarization curves (*iR* corrected) showed the current density versus voltage (*J* versus *V*) for comparison of 1T′-D and 2H phase WS_2 along with Pt/C (20%) samples. Under the same current density of $J = 10$ mA/cm^2 for H_2 evolution, a low overpotential of 200 mV vs RHE is enough for 1T′-D WS_2 (Fig. 3a), while an overpotential of 290 mV vs RHE is required for 2H WS_2, suggesting a strong catalytic activity of 1T′-D WS_2. The superior HER activity was further proved by the smaller Tafel slopes of 1T′-D WS_2 (50.4 mV/dec) than that of 2H WS_2 (99.4 mV/dec), indicating the kinetics of the electrochemical hydrogen evolution on 1T′-D WS_2 was much faster than the 2H WS_2 (Fig. 3b). The excellent HER performance of the synthesized 1T′-D WS_2 (e.g. low overpotential at $J = 10$ mA/cm^2 and small Tafel slope) is comparable to or even better than the reported WS_2 based electrocatalysts (Table S1).

As compared in Fig. S7, Nyquist plots revealed a decreased charge transfer resistance (R_{ct}) for the 1T′-D WS_2 relative to the 2H WS_2 for the same mass loading. The electrochemical impedance spectroscopy (EIS) results confirmed that 1T′-D WS_2 possesses much smaller impedance, benefiting faster hydrogen evolution. We also compared the electrochemical surface area (ECSA) of obtained WS_2 samples by measuring the double-layer capacitance (C_{dl}). Fig. S8a,b showed the typical cyclic voltammograms (CVs) of 1T′-D WS_2 and 2H WS_2 taken with various scan rates (20, 40, 60 mV/s, etc.) in the region of 0.1–0.3 V (vs. RHE) in 0.5 M H_2SO_4. Current density differences ($\Delta J = J_a - J_c$) at 0.2 V (vs. RHE) were plotted against scan rates. The electrochemical double-layer capacitances, equivalent to the linear slopes in Fig. 3c, were used to represent and compare the ECSA of 1T′-D WS_2 and 2H WS_2. It was noteworthy that the C_{dl} of 1T′-D WS_2 (18.8 mF/cm^2) was higher than that of 2H WS_2 (8.9 mF/cm^2) for the same mass loading, suggesting the 1T′-D WS_2 possessed much larger active surface area and more active sites for hydrogen production.

To further investigate the mechanism for the higher catalytic performance of 1T′-D WS_2, we applied first-principles density functional theory (DFT, see the Supporting Information for details) to calculate the ΔG_{H^*}, the adsorption free energy of H* on surface and edge sites for 1T′ WS_2 and edge sites for 2H WS_2 (the surface for 2H WS_2 was not taken into account as active sites only distribute on the edge for 2H phase TMD) [10], which is an appropriate parameter to describe the HER performance. The optimal ΔG_{H^*} value of HER catalyst should approach zero, which could facilitate the charge transfer processes for both H* intermediate and H_2 formation [25]. As shown in Fig. 3d, the H atoms adsorb on the protruding S of 1T′ WS_2 in the surface region, and on both S and W in the edge region of 1T′ and 2H WS_2. The calculated ΔG_{H^*} patterns of 1T′ and 2H WS_2 are shown in Fig. 3e. The ΔG_{H^*} values for both surface and edge of 1T′ WS_2 are closer to zero, which explain a better HER initial activity from 1T′ WS_2 than 2H WS_2, consistent with the experiment results.

Additionally, we investigated the stability of 1T′-D WS_2 and 2H WS_2 by continuous HER operation for 12 h. As shown in Fig. 4a, the current density of 1T′-D WS_2 shows a slight 8% drop after a long period of 12 h of continuous operation under static overpotential of 0.3 V vs. RHE. By comparison, the 2H WS_2 electrocatalyst exhibits a continuous decrease of 26% in HER activity after 12 h (Fig. 4a) under static overpotential of 0.45 V vs. RHE. Note here, the initial current density on 1T′-D WS_2 electrode is 41 mA/cm^2, higher than the 37 mA/cm^2 on the 2H WS_2 electrode. The possible reason for the dramatic decrease of 2H WS_2 HER activity resulted from oxidization of WS_2 to WO_x as HER proceeded, which was confirmed by the XPS spectra of W after stability testing (Fig. S9a). And we verified that the obtained WO_x by direct oxidation of 2H WS_2 displayed poor HER performance (Fig. S9b). In stark contrast, the XPS spectra of 1T′-D WS_2 after 12 h HER stability testing showed no obvious changes of the chemical state for W (Fig. S9c), indicating the 1T′-D WS_2 catalyst still maintained the 1T′ phase, and hence the excellent HER stability.

1T′-D WS_2 exhibited impressive HER stability, but what is curious about this material is why it still got 8% drop in performance after 12 h stability testing. In order to investigate the reason behind the slight HER degradation of 1T′-D WS_2, we compared the *ex*-situ XPS spectra of S recorded from 1T′-D WS_2 (Fig. 4b) at different times during the course of HER stability testing. Compared with pristine 1T′-D WS_2, it was found that a new strong peak appears at 169.1 eV after HER stability testing. The new peak is attributed to sulfonate. The formation of sulfonate can be further demonstrated by the FTIR spectra (Fig. 4c). The peaks at 1105 cm^{-1} and 987 cm^{-1} were indexed to S=O stretch and S-O stretch of sulfonate, respectively. However, we used Nafion

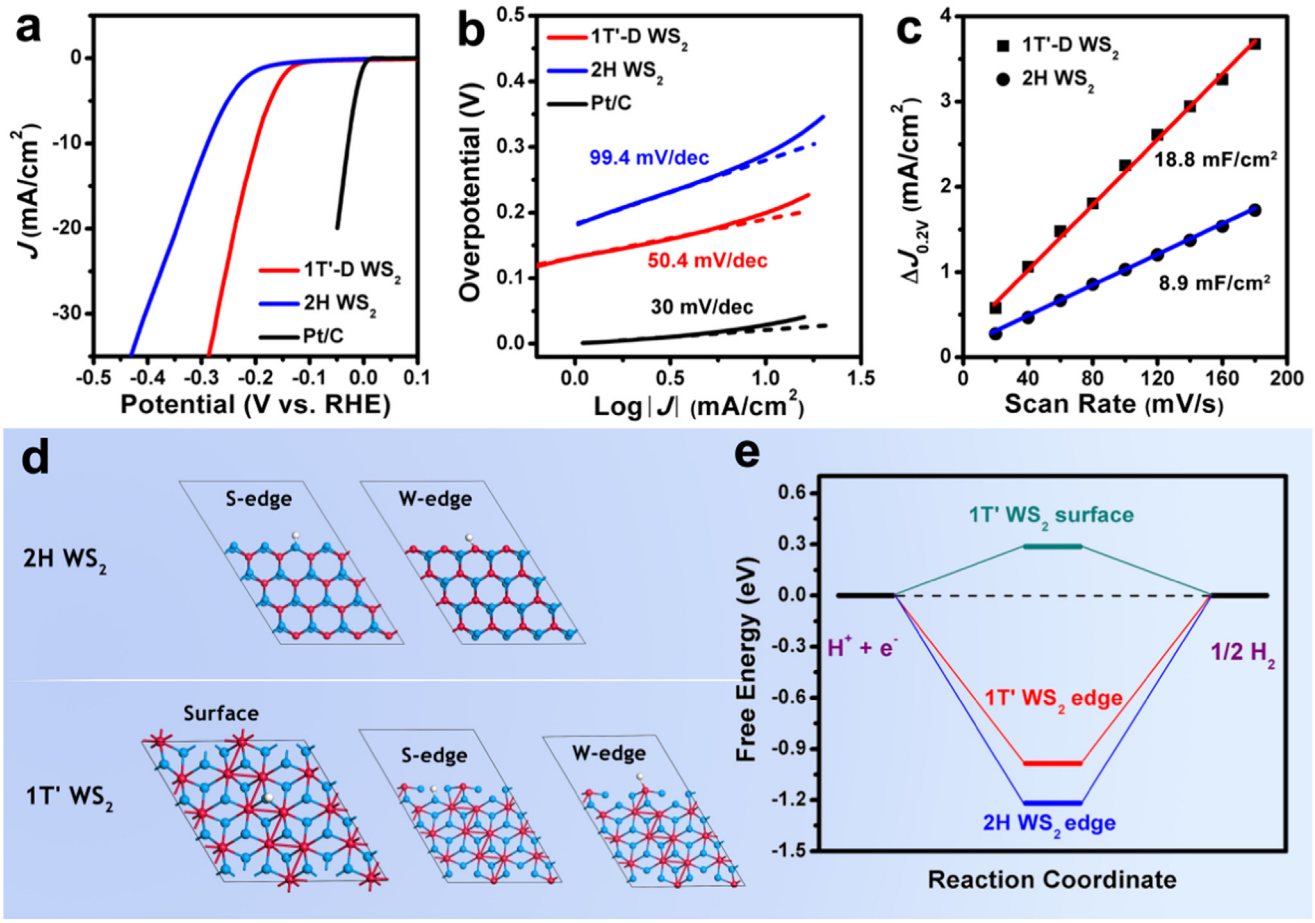

Fig. 3. (a) Polarization curves of 1T′-D WS_2, 2H WS_2, and commercialized Pt/C (20%) for comparison. "*J*" represents the current density. (b) The corresponding Tafel curves for catalysts derived from (a). (c) The electrochemically active surface area estimated from the voltammograms at various scan rates (20–180 mV/s, Fig. S8). (d) Surface and edge view of 1T′ and 2H phase WS_2. Red, blue and white balls represent W, S and H atoms, respectively. (e) The calculated free-energy diagram of HER for surface/edge of 1T′ and 2H phase WS_2.

(perfluorosulfonic acid-PTFE copolymer) as the fixative in the HER experiments. In order to rule out the possibility of sulfonate group from Nafion, we also studied PTFE (polytetrafluoroethylene) as fixative instead of Nafion in the HER experiment. As shown in Fig. 4c, we found that with either Nafion or PTFE, sulfonate could be generated during HER testing, thus it is not due to the fixative. The sulfonate may come from the reaction between WS_2's surface WO_x components and H_2SO_4 in 0.5 M H_2SO_4 electrolyte. Furthermore, during the HER operation, there still exists the transformation of 1T′-D phase to 2H phase (Fig. 4b). Therefore, the aforementioned causes the slight HER degradation of 1T′-D WS_2 after 12 h operation.

As a proof-of-concept demonstration, we implemented HER endurance testing to calculate the endurance half-life of electrocatalyst. As shown in Fig. 4d, the catalyst exhibited a relative stable HER activity in the first 5 days and then gradually decreased in course of HER stability testing (Fig. 4d). The high decrease rate after 15 days may result from WS_2 catalyst's mechanical peeling off the electrode after long-time immersion in the electrolyte, accelerated by erosion due to continuous H_2 bubbling from catalyst as observed from experiments that exert large capillary forces on the atomic sheets. The half-life of this HER could be calculated by the following Eq. (1):

$$t_{\frac{1}{2}} = \frac{t}{\log_{\frac{1}{2}}(\frac{N(t)}{N_0})} \quad (1)$$

where $t_{1/2}$ and t represent half-life and the variable of time, respectively. $N(t)$ and N_0 stand for the current density at time t and initial current density, respectively. Based on the definition of Eq. (1), the calculated half-life of 1T′-D WS_2 was about 46 days under constant overpotential of 0.3 V vs. RHE and an initial current density of 41 mA/cm^2. The XPS spectra of W and S recorded from the 1T′-D WS_2 catalyst after HER endurance testing over one month indicated that there were only WO_x species (Fig. S10a) and sulfonate left (Fig. S10b). This reveals another cause of HER performance degradation under high-current-density testing for 1T′-D WS_2 (Fig. 4d). As far as we know, this is the first long-term HER endurance test to evaluate the half-life of TMD electrocatalyst, which provides valuable experimental information on device lifetime and cost/performance tradeoff, thus benefiting the future research efforts towards industrialization.

3. Conclusion

In summary, we have established a one-pot colloidal synthesis method for selectively preparing metallic 1T′-D and semiconducting 2H phase WS_2 nanostructures with a high degree of monodispersity. After acid treatment, 1T′-D WS_2 largely remained and exhibited superior HER performance, such as low overpotential of 200 mV at current density 10 mA/cm^2, a small Tafel slope of 50.4 mV/dec and outstanding stability, compared with 2H WS_2. While the raw-materials cost limit of WS_2 (~ $100/kg) is much cheaper than that of Pt (~ $30,000/kg), if the endurance time of 1T′-D WS_2 is very short, it will never be able to compete with Pt-based HER catalysts. Here we have shown that at a very high current density of 41 mA/cm^2, our 1T′-D WS_2 catalyst is still super endurable, despite vigorous mechanical erosion by the bubbling H_2 gas and unavoidable chemical transformations to WO_x and

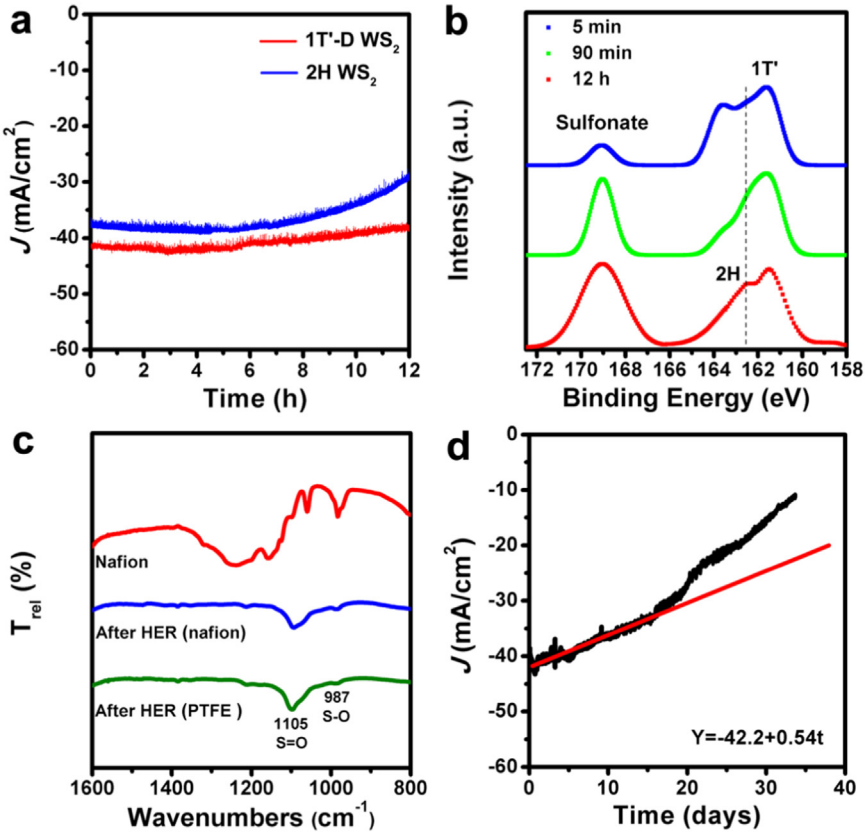

Fig. 4. (a) Continuous HER recorded from 1T′-D WS_2 and 2H WS_2 coated carbon fibre cloth (CFC) as working electrodes at a static overpotential of 0.3 V and 0.45 V vs. RHE, respectively. XPS spectra of (b) S2p recorded from 1T′-D WS_2 at different time in course of HER stability testing. (c) FTIR spectra of Nafion and 1T′-D WS_2 after HER test using Nafion and PVDF as a fixative. (d) Half-life time calculated by analysis continuous HER stability testing of 1T′-D WS_2 at a static overpotential of 0.3 V vs. RHE.

sulfonate. We believe our facile and scalable approach could be extended to selectively preparing 1T′ and 2H phases for other TMDs materials with various properties, in pursuit of cost-effectiveness for a wide range of applications, including the hydrogen economy.

Acknowledgments

We gratefully acknowledge the financial aid from the National Key R&D Program of China (2017YFA0208000), the China National Funds for Excellent Young Scientists (grant no. 21522106), the Starting Research Fund from Nankai University, the United States National Science Foundation (Grant No. ECCS-1610806) and the ANU Futures Scheme (Grant No. Q4601024).

Appendix A. Supporting information

Supplementary data associated with this article can be found in the online version at http://dx.doi.org/10.1016/j.nanoen.2018.05.019.

References

[1] M.G. Walter, E.L. Warren, J.R. McKone, S.W. Boettcher, Q. Mi, E.A. Santori, N.S. Lewis, Chem. Rev. 110 (2010) 6446–6473.
[2] C. Tan, X. Cao, X.-J. Wu, Q. He, J. Yang, X. Zhang, J. Chen, W. Zhao, S. Han, G.-H. Nam, M. Sindoro, H. Zhang, Chem. Rev. 117 (2017) 6225–6331.
[3] M.A. Lukowski, A.S. Daniel, C.R. English, F. Meng, A. Forticaux, R.J. Hamers, S. Jin, Energy Environ. Sci. 7 (2014) 2608–2613.
[4] D. Voiry, H. Yamaguchi, J. Li, R. Silva, D.C.B. Alves, T. Fujita, M. Chen, T. Asefa, V.B. Shenoy, G. Eda, M. Chhowalla, Nat. Mater. 12 (2013) 850–855.
[5] M.A. Lukowski, A.S. Daniel, F. Meng, A. Forticaux, L. Li, S. Jin, J. Am. Chem. Soc. 135 (2013) 10274–10277.
[6] L. Cheng, W. Huang, Q. Gong, C. Liu, Z. Liu, Y. Li, H. Dai, Angew. Chem. Int. Ed. 53 (2014) 7860–7863.
[7] B. Hinnemann, P.G. Moses, J. Bonde, K.P. Jørgensen, J.H. Nielsen, S. Horch, I. Chorkendorff, J.K. Nørskov, J. Am. Chem. Soc. 127 (2005) 5308–5309.
[8] D. Kong, H. Wang, J.J. Cha, M. Pasta, K.J. Koski, J. Yao, Y. Cui, Nano Lett. 13 (2013) 1341–1347.
[9] D. Merki, S. Fierro, H. Vrubel, X. Hu, Chem. Sci. 2 (2011) 1262–1267.
[10] S.S. Chou, N. Sai, P. Lu, E.N. Coker, S. Liu, K. Artyushkova, T.S. Luk, B. Kaehr, C.J. Brinker, Nat. Commun. 6 (2015) 8311.
[11] M. Acerce, D. Voiry, M. Chhowalla, Nat. Nanotechnol. 10 (2015) 313–318.
[12] Q. Liu, X. Li, Z. Xiao, Y. Zhou, H. Chen, A. Khalil, T. Xiang, J. Xu, W. Chu, X. Wu, J. Yang, C. Wang, Y. Xiong, C. Jin, P.M. Ajayan, L. Song, Adv. Mater. 27 (2015) 4837–4844.
[13] Q. Liu, X. Li, Q. He, A. Khalil, D. Liu, T. Xiang, X. Wu, L. Song, Small 11 (2015) 5556–5564.
[14] B. Mahler, V. Hoepfner, K. Liao, G.A. Ozin, J. Am. Chem. Soc. 136 (2014) 14121–14127.
[15] S.J.R. Tan, I. Abdelwahab, Z. Ding, X. Zhao, T. Yang, G.Z.J. Loke, H. Lin, I. Verzhbitskiy, S.M. Poh, H. Xu, C.T. Nai, W. Zhou, G. Eda, B. Jia, K.P. Loh, J. Am. Chem. Soc. 139 (2017) 2504–2511.
[16] L. Rapoport, Y. Bilik, Y. Feldman, M. Homyonfer, S.R. Cohen, R. Tenne, Nature 387 (1997) 791–793.
[17] S. Jo, N. Ubrig, H. Berger, A.B. Kuzmenko, A.F. Morpurgo, Nano Lett. 14 (2014) 2019–2025.
[18] X. Zong, J. Han, G. Ma, H. Yan, G. Wu, C. Li, J. Phys. Chem. C 115 (2011) 12202–12208.
[19] D. Yang, S.J. Sandoval, W.M.R. Divigalpitiya, J.C. Irwin, R.F. Frindt, Phys. Rev. B 43 (1991) 12053–12056.
[20] X. Geng, W. Sun, W. Wu, B. Chen, A. Al-Hilo, M. Benamara, H. Zhu, F. Watanabe, J. Cui, T.P. Chen, Nat. Commun. 7 (2016) 10672.
[21] L. Wang, X. Liu, J. Luo, X. Duan, J. Crittenden, C. Liu, S. Zhang, Y. Pei, Y. Zeng, X. Duan, Angew. Chem. Int. Ed. 56 (2017) 7610–7614.
[22] Y. Gao, X. Peng, J. Am. Chem. Soc. 136 (2014) 6724–6732.
[23] Q. Tang, D.E. Jiang, Chem. Mater. 27 (2015) 3743–3748.
[24] S.S. Chou, Y.K. Huang, J. Kim, B. Kaehr, B.M. Foley, P. Lu, C. Dykstra, P.E. Hopkins, C.J. Brinker, J. Huang, V.P. Dravid, J. Am. Chem. Soc. 137 (2015) 1742–1745.
[25] J.K. Nørskov, T. Bligaard, A. Logadottir, J.R. Kitchin, J.G. Chen, S. Pandelov, U. Stimming, J. Electrochem. Soc. 152 (2005) 23–26.

Colloidal Synthesis of 1T' Phase Dominated WS_2 Towards Endurable Electrocatalysis

Zhengqing Liu[a], Na Li[b], Cong Su[c], Hongyang Zhao[b], Lingling Xu[b], Zongyou Yin[d], Ju Li[c]*, and Yaping Du[a,b]**

[a] School of Materials Science and Engineering & National Institute for Advanced Materials, Nankai University, Tianjin 300350, China.

[b] Frontier Institute of Science and Technology, Xi'an Jiaotong University, Xi'an 710049, China.

[c] Department of Nuclear Science and Engineering and Department of Materials Science and Engineering, Massachusetts Institute of Technology, Cambridge, Massachusetts 02139, USA.

[d] Research School of Chemistry, the Australian National University, Canberra, Australian Capital Territory 2601, Australia.

* E-mail: ypdu@nankai.edu.cn

* E-mail: zongyou.yin@anu.edu.au

* E-mail: liju@mit.edu

Experimental Section

Chemicals. Ammonium tungsten oxide ($(NH_4)_2WO_4$, 99.99+%, Alfa Aesar), thiourea (CH_4N_2S, >99.0%, Sigma-Aldrich), oleylamine (OM, 70%, Sigma-Aldrich), oleic acid (OA, 90%, Sigma-Aldrich), ethanol (AR), and cyclohexane (AR) were used as received without further purification.

Synthesis of metallic 1T' phase dominated WS_2 nanoparticles (NPs), referred to as 1T'-D WS_2. Typically, 0.2 mmol $(NH_4)_2WO_4$ and 0.6 thiourea were added to a 100 mL three-neck flask containing 20 mmol OM at room temperature. Then, the slurry was heated to 120 ºC in vacuum for about 30 min to remove water and oxygen. The resulting solution was rapidly heated to 280 ºC and vigorously stirred for 90 min under N_2 atmosphere. When the reaction was completed, the nanocrystals were precipitated with ethanol (AR). The as-obtained 1T'-D WS_2 were washed 3 times with cyclohexane (AR) and ethanol by centrifugation at 8,500 rpm before drying overnight in a vacuum oven at 60 ºC.

Synthesis of 2H phase WS_2 nanochains, referred to as 2H WS_2. The synthetic procedure was similar to that used for the synthesis of 1T'-D WS_2 NPs except for 16 mmol OM and 4 mmol OA were used as solvents for reaction at 280 ºC for 60 min.

Characterizations. Scanning electron microscope (SEM) images were characterized by a Quanta F250. TEM images were acquired from a Hitachi HT-7700 transmission electron microscope (TEM, Japan) operating at 100 kV. High-resolution TEM (HRTEM) micrographs were obtained with a Philips Tecnai F20 FEG-TEM (The USA) operated at 200 kV. Samples for TEM analysis were prepared by drying a drop of a cyclohexane solution containing the nanomaterials on the surface of a carbon-coated copper grid. The X-ray diffraction XRD patterns were obtained using a Rigaku D/MAX-RB with monochromatized Cu Kα radiation (λ=1.5418

Å) in the 2θ ranging from 5° to 80°. Infrared spectra were recorded on a Nicolet 6700 FTIR spectrometer. X-ray photoelectron spectra (XPS) were conducted using a PHI Quantera SXM instrument equipped with an Al X-ray excitation source (1486.6 eV). Binding energies of spectra were referenced to the C 1s binding energy set at 284.6 eV. UV-vis absorption spectra were measured on a Perkin-Elmer Lambda 35UV-vis spectrophotometer. Raman spectra of powder samples were recorded on LabRAM HR Raman microscope with a laser excitation wavelength of 532 nm. Inductively Coupled Plasma-Optical Emission Spectrometer (ICP-OES) was taken on Perkin Elmer Optima 5300DV. The synthesized WS_2 samples were dissolved in aqua regia and diluted with water for ICP-OES determination of the ratio of W and S.

Electrocatalytic measurements for HER. Before the electrochemical test, the fresh as-prepared 1T'-D WS_2 product was added into a 100 mL Erlenmeyer flask containing 3 mL thioglycolic acid and 50 mL ethanol, and vigorously stirred for 12 h under N_2 atmosphere to partially removing the surfactant molecules [1]. After that, the acid-treated 1T'-D WS_2 samples were separated from the solution by centrifugation (8,500 rpm, 10 min), washed twice with ethanol, and re-dispersed in the mixed ethanol-isopropanol solution (v/v = 1/1) containing 0.4 wt.% of Nafion. Then, 5.0 μL of 1T'-D phase WS_2 solution (containing 20 μg of catalyst, determined by the inductive coupled plasma-optical emission spectroscopy) was dropped onto the surface of cleaned GCE and dried overnight naturally. The 2H WS_2 product was annealed in forming gas (5% H_2 + 95% Ar) at 200 ºC for 2 h to remove the organic residue (such as OM and OA). Then 2H WS_2 work electrodes were prepared by the same method with 1T'-D WS_2 work electrodes. Linear sweep voltammetry was carried out in 0.5 M H_2SO_4 (deaerated by N_2) with a scan rate of 5 mV/s using a graphite electrode as the counter electrode, a saturated calomel ($Hg/HgCl_2$ in saturated KCl) as the reference electrode and the rotating disk glassy carbon electrode as the working electrode

with a rotating speed of 1,600 rpm. All the potentials were converted to values with reference to a reversible hydrogen electrode (RHE). Cyclic voltammograms (CVs) were conducted at room temperature by using the same standard three-electrode setup with various scan rates (20, 40, 60 mV/s, etc.). Nyquist plots of three samples were measured in the frequency range from 100 Hz to 0.1 kHz at an open circuit potential of -350 mV. 1T'-D WS_2 and 2H WS_2 -coated carbon fiber cloth (CFC) (0.5 cm^2, catalyst loading 140 μg) were used as working electrodes to collect chronoamperometry data at the applied potential of -0.3 V and -0.45 V vs. RHE, respectively.

Theoretical calculation. The density functional theory (DFT) calculations of the hydrogen adsorption on 2H and 1T' phase WS_2 were performed by using the DMol3. All energies were calculated with Perdew, Burke, and Ernzerhof (PBE) of generalized gradient approximation (GGA). The convergence threshold for structural optimization and energies were set to be 10^{-6} eV/Å in force. We apply G-centered 2×2×1 k-points grids for Brillouin zone sampling of all calculations. The configurations of hydrogen adsorption were calculated using the 4×4×1 supercells. The single-layered WS_2 was modeled using surface and edge supercells separated in the periodic direction by a 15 Å-thick vacuum slab. For the surface, the most stable H binding site in the basal plane of WS_2 is on the top of the S atoms. For the edge, we have examined two possible sites with high symmetry S-top site and W-top site of H adsorption. The H coverage considered in the calculations is 6.25%. The free energy change for H* adsorption on WS_2 surface and edge (ΔG_{H^*}) was calculated as follows, which is proposed by Norskov and coworkers [2]:

$$\Delta G_{H^*} = E_{total} - E_{WS_2} - \frac{E_{H_2}}{2} + \Delta E_{ZEP} - T\Delta S$$

where E_{total} is the total energy for the adsorption state, E_{WS_2} is the energy of pure surface or edge, E_{H_2} is the energy of H_2 in the gas phase, ΔE_{ZEP} is the zero-point energy change and ΔS is the entropy change. Thus, (ΔE_{ZEP}-$T\Delta S$) is simplified as 0.27 eV, where 0.27 eV is the contribution from ZPE and entropy at 298 K.

Results and Discussion

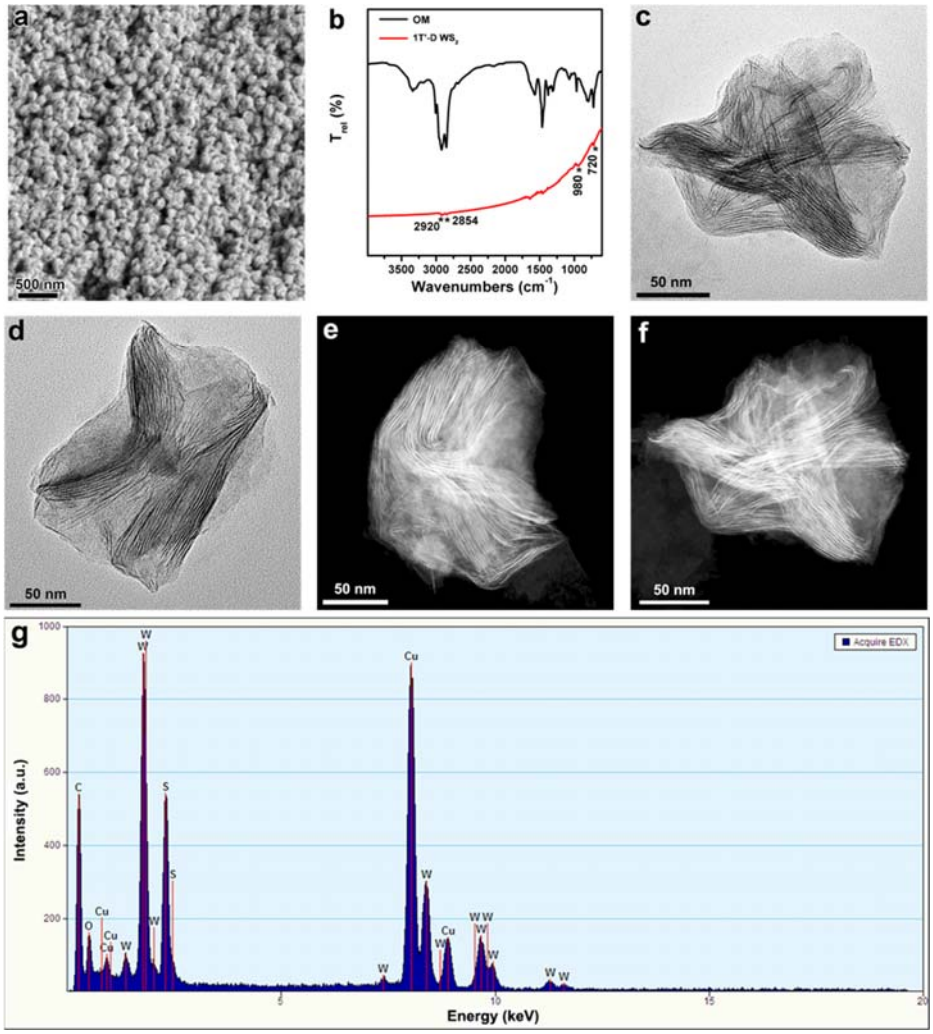

Fig. S1. (a) SEM image of obtained 1T'-D WS_2 NPs. (b) FTIR spectra of OM and 1T'-D WS_2 NPs. The presence of acyclic C–H stretching at 2920 cm^{-1} and 2854 cm^{-1} indicates the existence OM. The two peaks at 980 cm^{-1} and 720 cm^{-1} were indexed to C–N stretch of OM. Based on the FTIR analysis, it was confirmed that the 1T'-D WS_2 NPs were coated by OM organic molecule [3]. A single (c,d) TEM and (e,f) HAADF-STEM images of the 1T'-D WS_2 NPs. (g) Energy-dispersive X-ray analysis (EDX) spectrum of 1T'-D WS_2 NPs.

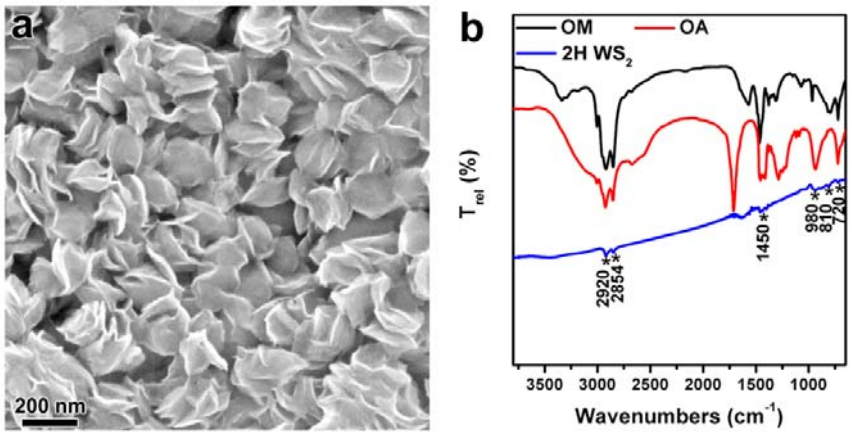

Fig. S2. (a) SEM images of the as-prepared 2H WS_2 NCs. (b) FTIR spectra of OM, OA, as-prepared 2H WS_2 NCs. The presence of acyclic C–H stretching at 2920 cm^{-1} and 2854 cm^{-1} indicate the co-existence of OA and OM. The peaks at 1450 cm^{-1} is assigned to C=O stretch and carboxylate (COO^-) stretch, implying the COO^- ligand exists on the nanostructures' surface. Additionally, the three peaks at 980 cm^{-1}, 810 cm^{-1}, and 720 cm^{-1} for 2H WS_2 NCs are indexed to C–N stretch of OM. Based on the FTIR analysis of 2H WS_2 NCs, it is confirmed that these 2H WS_2 NCs are coated with two kinds of organic capping ligands, OM and OA [3].

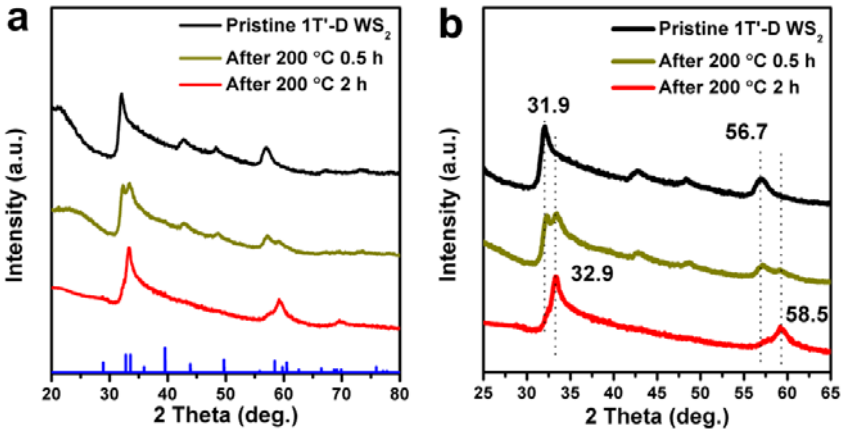

Fig. S3. XRD patterns of (a) 1T'-D WS_2 NPs during the thermal treatment process. (b) Enlarged XRD patterns recorded from (a).

The influence of $(NH_4)_2WO_4$ precursor concentration and thiourea concentration for colloidal synthesis of 1T'-D WS_2 NPs: fixing the mole ratio of $(NH_4)_2WO_4$ to thiourea (1:3), volume of solvents, reaction temperature and time, when using 0.1 mmol $(NH_4)_2WO_4$ and 0.3 mmol thiourea in 20 mmol OM for a reaction at 280 °C for 90 min, we only got aggregated nanosheets without WS_2 NPs morphologies (Fig. S4a). Under the same reaction condition, except increasing $(NH_4)_2WO_4$ amount to 0.2 mmol and thiourea amount to 0.6 mmol resulted in monodispersed WS_2 NPs (Fig. 1a). While further increasing $(NH_4)_2WO_4$ amount to 0.3 mmol and thiourea amount to 0.9 mmol produced aggregated WS_2 NPs with low yield (Fig. S4b). In addition, the concentration of thiourea was also found to play a crucial role in the formation of high-quality WS_2 NPs. As shown in Fig. S4c,d, no matter the concentration of thiourea lower or higher than 0.6 mmol, the monodispersed WS_2 NPs could not be harvested. To conclude, the concentration of 0.2 mmol $(NH_4)_2WO_4$ and 0.6 mmol thiourea in 20 mmol OM at 280 °C for 90 min was proper for the preparation of high-quality 1T'-D WS_2 NPs.

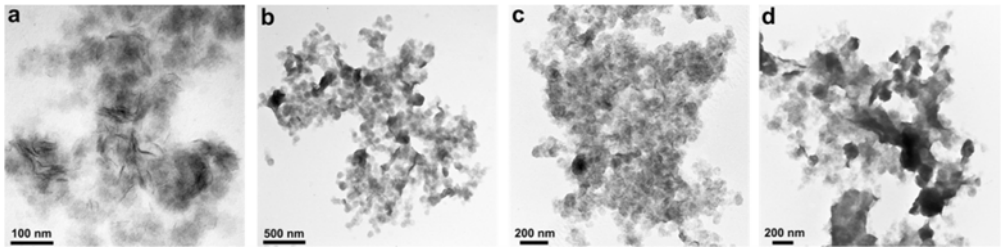

Fig. S4. TEM images of 1T'-D WS_2 products formed from the reaction with different precursor concentration of $(NH_4)_2WO_4$ and thiourea in 20 mmol of OM in a 100 mL three-neck flask at 280 ºC for 90 min: (a) $(NH_4)_2WO_4$ (0.1 mmol): thiourea (0.3 mmol) = 1:3; (b) $(NH_4)_2WO_4$ (0.3 mmol): thiourea (0.9 mmol) = 1:3; (c) $(NH_4)_2WO_4$ (0.2 mmol): thiourea (0.4 mmol) = 1:2; and (d) $(NH_4)_2WO_4$ (0.2 mmol): thiourea (0.8 mmol) = 1:4.

The influence of solvents ratio of OM/OA for colloidal synthesis of 2H WS_2 NCs: In the present work, when the ratio of OM/OA was 1:1, the by-products of WO_3 appeared (Fig. S5d,e). High yields of self-assembled chain-like WS_2 nanostructures were only harvested at an optimized OM/OA ratio of 4:1 at 280 °C for 60 min (Fig.1f vs. S5).

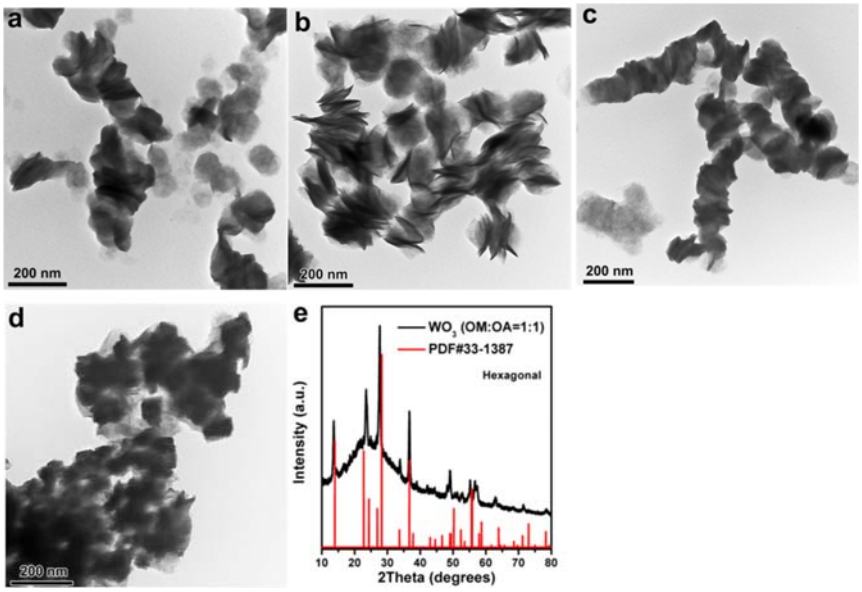

Fig. S5. TEM images of 2H WS_2 NCs formed from the 0.2 mmol of $(NH_4)_2WO_4$ and 0.6 mmol thiourea with different mixed solvents (OM/OA) in a 100 mL three-neck flask at 280 ºC for 60 min: (a) OM/OA=9:1, (b) OM/OA =6:1, (c) OM/OA =2:1, and (d) OM/OA =1:1. (e) The corresponding XRD pattern of (d) product.

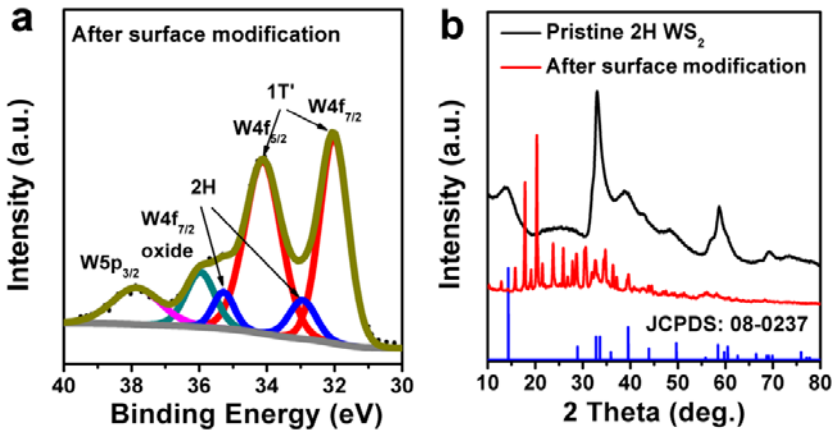

Fig. S6. The (a) XPS spectra of 1T'-D WS_2 after surface modification. The (b) XRD patterns of 2H WS_2 after surface modification.

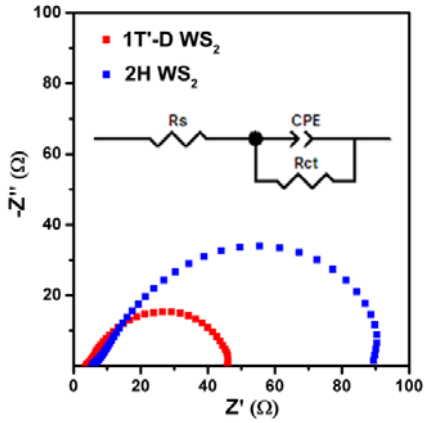

Fig. S7. EIS Nyquist plots collected at a bias voltage of -350 mV showing the electrode kinetics of the 1T'-D WS_2 and 2H WS_2. Inset: the fitted equivalent circuit of 1T'-D WS_2, where a constant phase element (CPE) was employed. Nyquist plots revealed a decreased charge transfer resistance (R_{ct}) for the 1T'-D WS_2 (41.9 Ω) relative to the 2H WS_2 (84.2 Ω).

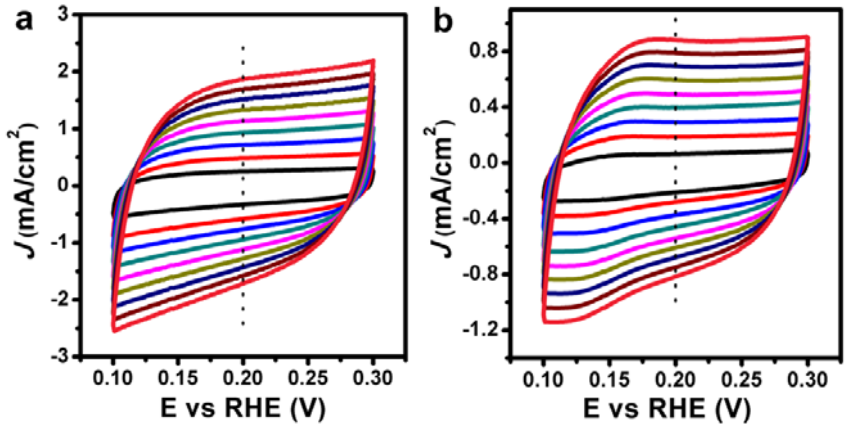

Fig. S8. Voltammograms of the (a) 1T'-D WS_2 and (b) 2H WS_2 electrocatalysts at various scan rates (20-180 mV/s). "*J*" represents the current density.

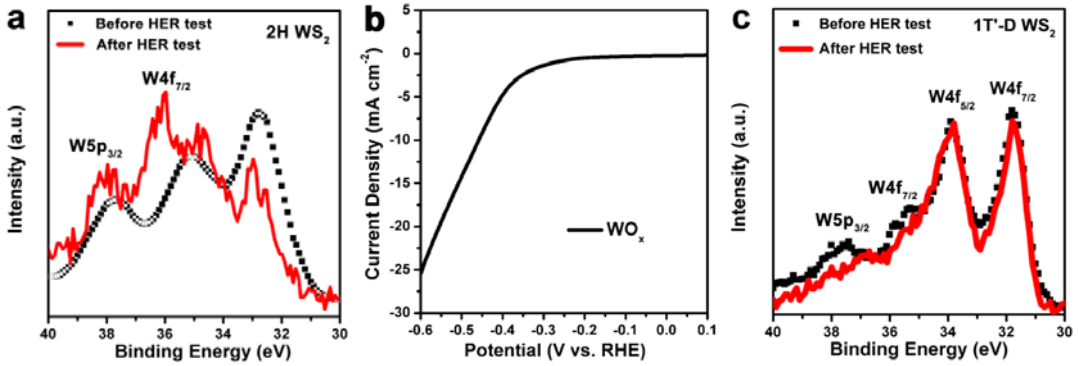

Fig. S9. (a) The comparison of XPS spectra of W for 2H WS_2 before and after continuous HER process. The enhanced intensity of $W5p_{3/2}$ at 37.5 eV and $W4f_{7/2}$ at 35.4 eV suggested partial oxidation of 2H WS_2 as a result of HER in 0.5 M H_2SO_4 electrolyte. (b) LSV curve of WO_x electrocatalyst by oxidation of 2H WS_2. (c) The comparison of XPS spectra of W for 1T'-D WS_2 before and after continuous HER process.

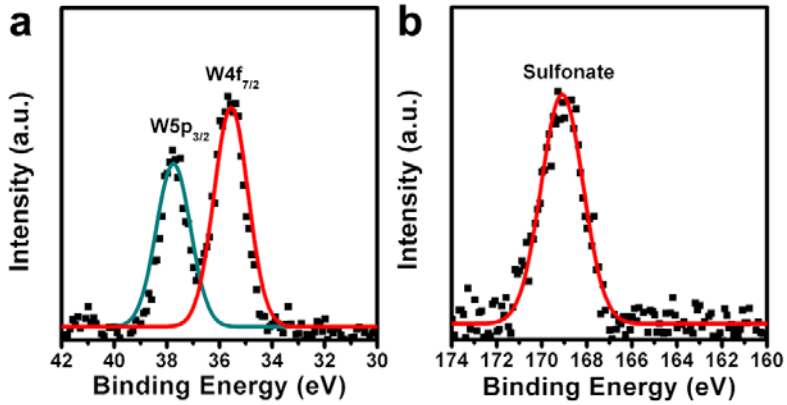

Fig. S10. XPS spectra of (e) W4f and (f) S2p for 1T'-D WS_2 after continuous HER stability testing of Fig. 4d.

Table S1. Summary of the HER performance using WS_2 nanostructures as electrocatalysts.

Catalyst	Overpotential at $J = 10$ mA/cm^2	Tafel Slope (mV/dec)	Stability Time/CV cycles	Reference
1T'-D/2H WS_2	**200 (1T'-D)** **290 (2H)**	**50.4 (1T'-D)** **99.4 (2H)**	**5 days (1T'-D)** **6 h (2H)**	**Our work**
WS_2 nanodots WS_2 nanosheets	209 310	63 95	- -	*Adv. Mater.* **2018**, *30*, 1705509.
WS_2@ordered mesoporous carbon nanocomposites	213	74	20 h	*Nanoscale* **2018**, *10*, 3838.
Monolayer dendritic $WS_{2(1-x)}Se_{2x}$ flakes	156	69	1000 cycles	*Nanoscale* **2017**, *9*, 5641.
$WS_{2(1-x)}P_{2x}$ nanoribbons	98	71	1000 cycles	*Small* **2017**, *13*, 1603706.
Exfoliated WS_2 nanosheets	225	73	1000 cycles	*Nanoscale* **2017**, *9*, 13515.
WS_2 nanosheets	278	120	-	*J. Phys. Chem. C* **2016**, *120*, 3929.
WS_2 nanorattle	192	68	5000 cycles	*J. Power Sources* **2016**, *307*, 593.
WS_2/WS_3 film	494	43.7	100 cycles	*ACS Appl. Mater. Interfaces* **2016**, *8*, 3948.
N-doped WS_2 nanosheets	ca. 160	69	5000 cycles	*J. Mater. Chem. A* **2016**, *4*, 11234.
3D WS_2@P,N,O doped-graphene nanocomposites	125	52.7	20 h	*Adv. Mater.* **2015**, *27*, 4234.
$W_{18}O_{49}$@WS_2 core-shell nanorods	310	86	-	*Chem. Commun.* **2015**, *51*, 8334.
WS_2/rGO hybrid nanosheets	195	52	3000 cycles	*Nanoscale* **2015**, *7*, 10391.
WS_2/N-doped carbon nanofibers nanocomposites	ca. 280	60	6 h	*ACS Appl. Mater. Interfaces* **2015**, *7*, 28116.
Monolayer WS_2 nanosheets on Au foils	350	100	1000 cycles	*Nano Res.* **2015**, *8*, 2881.
rGO/WS_2 nanocomposites	229	73	-	*Nanoscale* **2015**, *7*, 14760.
WS_2 Quantum Dots	350	70	-	*Adv. Funct. Mater.* **2015**, *25*, 1127.

$WS_{2(1-x)}Se_{2x}$ nanotubes	ca. 300	105	2 h	*ACS Nano* **2014**, *8*, 8468.
WS_2 nanoribbons	240	68	1000 cycles	*Adv. Energy Mater*. **2014**, *4*, 1301875.
Ultrathin WS_2 nanoflakes	ca. 180	48	10,000 cycles	*Angew. Chem. Int. Ed.* **2014**, *53*, 7860.
Metallic WS_2 nanosheets	142	70	4 h/500 cycles	*Energy Environ. Sci.* **2014**, *7*, 2608.
WS_2/rGO nanocomposites	ca. 280	58	None	*Angew. Chem. Int. Ed.* **2013**, *52*, 13751.
WS_2/Au nanocomposites	ca. 380	57	None	*J. Phys. Chem. Lett.* **2013**, *4*, 1227.
Strained WS_2 nanosheets	ca. 250	60	100 h/10,000 cycles	*Nat. Mater*. **2013**, *12*, 850.
WS_2 nanoflakes	ca. 350	200	None	*Nano Res.* **2013**, *6*, 921.
$CoWS_x$	373	78	1 h	*Energy Environ. Sci*., **2013**, *6*, 2452.
WS_2/carbon cloth	214	68	3 h	*Int. J. Hydrogen Energy*, **2013**, *38*, 12302.
WS_2 nanosheets	ca. 160	72	10,000 cycles	*Appl. Catal. B* **2012**, *125*, 59.

References

[1] a) V. Mazumder, M. Chi, K. L. More, S. Sun, *J. Am. Chem. Soc*. **2010**, *132*, 7848-7849; b) Q. Tang, D. E. Jiang, *Chem. Mater*. **2015**, *27*, 3743-3748.
[2] J. K. Nørskov, T. Bligaard, A. Logadottir, J. Kitchin, J. G. Chen, S. Pandelov, U. Stimming, *J. Electrochem. Soc*. **2005**, *152*, 23-26.
[3] A. L. Willis, N. J. Turro, S. O'Brien, *Chem. Mater*. **2005**, *17*, 5970-5975.